Fracture-mediated deep seawater flow and mantle hydration on oceanic transform faults

Cécile Prigent, J.M. Warren, A.H. Kohli, C. Teyssier

Fracture-mediated deep seawater flow and mantle hydration on oceanic transform faults

C. Prigent [a*], J.M. Warren [a], A.H. Kohli [b], C. Teyssier [c]

[a] Department of Geological Sciences, University of Delaware, Penny Hall, 255 Academy Street, Newark, Delaware 19716, U.S.A.

[b] Department of Geophysics, Stanford University.

[c] Department of Geology and Geophysics, University of Minnesota.

* Corresponding author

Email address: cprigent@udel.edu

To be submitted to *Earth and Planetary Science Letters*

5941 Words

7 Figures

2 Tables

65 Citations

Abstract

Fluid-rock interaction on oceanic transform faults (OTFs) is important for both the deformation behavior of the lithosphere and volatile cycling in the Earth. Rocks deformed and exhumed at OTFs preserve information about the depth extent of fluid percolation and the nature of fluid-rock interactions within these fault zones. In this study, we focus on five dredges from the Shaka and Prince Edward OTFs on the ultraslow spreading Southwest Indian Ridge that recovered significant volumes of deformed mantle rocks. Samples are predominantly mylonites that have been deformed to high strains in the fault zone, but also contain several generations of fractures. Based on the mineral assemblages in fractures and shear bands combined with thermobarometry analysis, we identified three distinct temperature ranges of fluid-mantle interactions associated with deformation. At low temperature (LT), this leads to crystallization of serpentine (± talc ± amphibole ± chlorite) at <500-550°C. At medium temperature (MT), chlorite and amphibole crystallized at ~500-750°C. At high temperature (HT), amphibole (± second generation peridotitic minerals) crystallized. The composition of minerals in HT fractures and shear bands indicate that fracturing and fluid flow occur up to temperatures of at least 850-875°C. Combining these results with modeled geotherms for both faults suggests that seawater percolation extended to depths of 20-25 km and that serpentinization extended to ~11-13 km. The evolution of fault zone structure induced by deep fluid-rock interaction and progressive formation of LT, MT and HT mylonites on OTFs results in weakening and strain localization within the oceanic lithosphere, and suggests that the global transform system may represent a large reservoir of volatiles in the Earth's lithosphere.

Keywords

Fluid-rock interaction; Peridotite; Mylonite; Oceanic transform fault; Southwest Indian Ridge; Serpentinization

1. Introduction

Fault zones serve as pathways for fluid migration through the lithosphere owing to enhanced permeability caused by brittle fracturing (e.g., Caine et al., 1996; Sibson et al., 1975) and ductile flow (e.g., Fusseis et al., 2009; McCaig, 1988). The resulting fluid-rock interactions and metamorphic reactions are crucial controls on the long-term mechanical behavior and composition of fault zones (Faulkner et al., 2010). For oceanic faults, which have an unlimited overlying supply of seawater, the extent of fluid flow controls both fault rheology and volatile cycling between the Earth's surface and the mantle (e.g., Hacker et al., 2003; Rüpke et al., 2004; Scambelluri et al., 2004).

At slow-spreading mid-ocean ridges, studies of fluid-rock interaction have shown that detachment faults are sites of enhanced fluid flow and mantle hydration. Hydrothermal fluids have been found to percolate down to 600-800°C (e.g., McCaig et al., 2010; Miranda and John, 2010; Picazo et al., 2012), corresponding to ~7 km depth on the Mid-Atlantic Ridge (MAR) (e.g., Hansen et al., 2013), resulting in mantle serpentinization up to ~400°C and crystallization of amphibole-chlorite-talc assemblages at higher temperatures (Picazo et al., 2012; Rouméjon and Cannat, 2014).

Observations from oceanic transform faults (OTFs) also suggest the occurrence of enhanced hydrothermal circulation and deep fluid flow within the fault zone. Seafloor exposures of exhumed mantle rocks along the Vema OTF on the MAR indicate that the upper mantle can be highly serpentinized at shallow depths (Boschi et al., 2013). The presence of syn-deformational amphibole at Vema (Cannat and Seyler, 1995; Cipriani et al., 2009) and at the Shaka OTF (Kohli and Warren, 2019) on the Southwest Indian Ridge (SWIR) suggests that seawater may percolate to even higher temperatures. Geophysical observations also indicate that some OTFs at intermediate and fast spreading ridges have negative gravity anomalies (Gregg et al., 2007; Pickle et al., 2009) and low seismic wave velocities compared to the surrounding lithosphere (Froment et al., 2014; Roland et al., 2012), both of which are interpreted as evidence of high porosity and/or extensive serpentinization of fault material. Studies of subduction zones where oceanic fracture zones are subducting have also

hypothesized that higher slab seismicity (Paulatto et al., 2017; Schlaphorst et al., 2016) and geochemical enrichments of arc volcano lavas erupting above these faults (e.g., Manea et al., 2014) could be due to enhanced hydration of the mantle on OTFs and their fracture zones.

Despite the potential importance of hydration of the oceanic lithosphere for OTF deformation and for the subduction zone water budget, limited work has been done to systematically characterize fluid-rock interactions on OTFs. Dredging campaigns along the SWIR ridge-transform system have recovered significant volumes of deformed mantle rocks (serpentinites and peridotite mylonites) in three dredges from the Shaka OTF and two dredges from the Prince (Pr.) Edward OTF. Microstructural analysis of four peridotite mylonites from Shaka (Kohli and Warren, 2019) revealed that some of the mylonites underwent relatively high temperature deformation and hydration within the fault zone prior to exhumation. In this paper, we focus on the full range of deformed mantle rocks that were recovered in the five SWIR dredges**.** We characterize sample mineralogy and chemistry to estimate the pressure-temperature-fluid-deformation path of mantle rocks, understand the nature of fluid-mantle interaction processes, and determine the depth extent of fluid percolation on OTFs. Finally, we assess the consequences of fluid-rock interaction processes for oceanic lithosphere composition and deformation.

2. Sample selection

The Shaka and Pr. Edward OTFs on the SWIR (Fig. 1) were sampled during two cruises in the 1980s. Cruise 107, leg 6, on the R/V Atlantis II in 1980 (Farmer and Dick, 1981) collected seven full and one empty dredges (60-67) across the Shaka OTF (Fig. 1d). The Protea expedition, leg 5, on the R/V Melville in 1984 (Fisher et al., 1985, 1986; Scripps Institution of Oceanography, 1984) collected four dredges (17-20) across the Pr. Edward OTF (Fig. 1e). Large amounts of peridotite mylonites were recovered in the five dredges that sampled the E-SE walls of each transform (60, 61, 63, 18 and 19), spanning a vertical distance of 1-3 km and a lateral extent of ~25 km.

From available multibeam bathymetry data (GMRT basemap v3.6), we constructed topographic profiles perpendicular to the trace of each fault (Figs. 1d-e). These profiles show that dredges containing peridotite mylonites were collected at distances ranging from <1 km up to ~7 km away from the deepest point in the transform fault valley. The mylonite-bearing dredges contain 29-100% ultramafic samples, with the remaining samples mainly consisting of basalts, diabases and greenstones (i.e., altered mafic rocks). We have not assessed the extent of deformation in the crustal lithologies; the sample descriptions from the cruise reports (Farmer and Dick, 1981; Scripps Institution of Oceanography, 1984) indicate that they have only been affected by brittle deformation. Among the ultramafic samples, 0-56% are porphyroclastic peridotites, 25-96% are mylonitic peridotites and 0-17% are foliated serpentinites (See Supplementary Table 1 for dredge sample descriptions). Breccias make up 0 to 9% of the dredges and exhibit either carbonate or serpentine matrices. All mantle rocks underwent intense deformation, mainly through ductile processes, but exhibit varying degrees of strain (i.e. grain size reduction). The proportion of highly deformed peridotites compared to protogranular and porphyroclastic peridotites decreases away from the center of the fault zone for both OTFs (Figs. 1d-e).

The samples used in this study come from the seafloor sample repository at Woods Hole Oceanographic Institution. From the five dredges that sampled the fault zones along the Shaka and Pr. Edwards OTFs, we classified the textures of 34 deformed samples. These samples were chosen as representative of the range of lithologies and textures found within each dredge (Supplementary Table 1). In the cruise reports, 10 samples were classified as porphyroclastic peridotites (from dredges 61, 63 and 19), 22 as mylonites (from dredges 60, 61 and 18) and 2 as serpentinites (dredge 61). Based on analysis of hand samples and thin sections, we re-classified all these samples as mylonites. Our updated descriptions along with the original dredge descriptions are in Supplementary Table 1. We then subdivided the samples into three groups based on the intensity of grain size reduction through the proportion of fine-grained matrix: <50% for protomylonites, 50-90% for mylonites and >90% for ultramylonites (e.g., Passchier and Trouw, 2005). In this classification, samples that were described as

122 porphyroclastic are now termed protomylonitic. Photos of the different mylonitic textures in hand
123 sample and thin section are shown in Figs. A1 and A2.

124 Of the 34 hand samples evaluated (Supplementary Table 1), 7 from Shaka and 4 from Pr.
125 Edward were selected for detailed geochemical analysis (Table 1). The samples represent four of the
126 five mylonite-bearing dredges and cover the range of observed textures. Samples from dredge 63 were
127 not selected for further analysis because they are too weathered.

128

129 # 3. Methods

130 ## 3.1. Sample mineralogy

131 We used a combination of optical microscopy and energy-dispersive X-ray spectroscopy (EDS)
132 analysis to determine sample mineralogy and phase distribution. For EDS analysis, we used a Zeiss
133 Auriga 60 CrossBeam scanning electron microscope (SEM) equipped with an Oxford Synergy X-
134 MAX 80 mm^2 EDS detector at the Keck Center for Advanced Microscopy at the University of
135 Delaware (USA). Measurements were made at an accelerating voltage of 15 kV, an aperture of 30 µm
136 (which controls the beam current) and a working distance of 8-10 mm. For EDS analyses, dwell time
137 and process time were set in order to get a deadtime of ~20%. AZtec v3.3 software from Oxford
138 Instruments (UK) was used to collect and process EDS spectra and to construct phase maps.

139

140 ## 3.2. Mineral composition

141 Quantitative compositional analysis of minerals was performed on two different electron microprobes:
142 a JEOL JXA-8900R at the Department of Earth Sciences, University of Minnesota (USA) and a JEOL
143 JXA-8230 at ISTerre, Grenoble-Alpes University (France). Data are reported in Supplementary Table
144 2.

145 At the University of Minnesota, data were collected with an accelerating voltage of 15 kV, a
146 beam current of 20 nA on a tungsten filament and beam diameters of 1 µm. The on-peak counting time

was 20 s for all elements and mean atomic number (MAN) backgrounds were utilized (Donovan et al., 2016). Standardization was made using synthetic and natural oxides as well as natural minerals. Unknown and standard intensities were corrected for deadtime and standard intensities were corrected for drift over time. The matrix correction was calculated with a Phi-Rho-Z method using an Armstrong/Love Scott algorithm (Armstrong, 1988) and the mass attenuation coefficients from the FFAST database (Chantler et al., 2005). Oxygen abundance was calculated by cation stoichiometry and included in the matrix correction.

At ISTerre, data were collected with an accelerating voltage of 20 kV and a field emission gun with a beam current of 300 nA for olivine (see detailed procedure in Sobolev et al., 2007), 20 kV and 50 nA for spinel, and 15 kV and 12 nA for other silicates. Beam diameters ranged from 1-5 µm depending on the target grain size. Standardization was made using synthetic oxides and natural minerals. The matrix correction was calculated with a ZAF method (e.g., Batanova et al., 2015).

3.3. Thermobarometry

To determine the P-T conditions during mylonite deformation, we used empirical thermometers to evaluate temperature and construct pseudosections to determine the stability fields of mineral assemblages associated with deformation. We applied two thermometers, both of which are based on orthopyroxene composition: $T_{Al\text{-}Cr\ in\ Opx}$ of Witt-Eickschen and Seck (1991) and $T_{Ca\ in\ Opx}$ of Brey and Köhler (1990). $T_{Ca\ in\ Opx}$ reported in Table 2 was calculated for a pressure of 5 kbars.

Pseudosections were constructed using Perple_X software (Connolly, 2009) in the NCFMASH (Na_2O-CaO-FeO-MgO-Al_2O_3-SiO_2-H_2O) chemical system. As whole rock major element compositions are needed to define the system composition, we obtained the composition of one protomylonite, three mylonites, and three ultramylonites through analysis of samples at the Washington State University GeoAnalytical Lab (Table B.1). Details of the thermodynamic solid solution models used in Perple_X are provided in Appendix B.

4. Results

All mylonites show both ductile and brittle deformation features. We classified the samples into three categories based on the mineral assemblages associated with their ductile deformation, which we interpret as representative of distinct temperature ranges of deformation (Table 1). We therefore term the categories as low-temperature (LT), medium-temperature (MT) and high-temperature (HT) mylonites (Fig. 2). This classification scheme is based primarily on mineralogy, so different rock textures from proto- to ultra-mylonite may be grouped together.

4.1. Petrographic observations of ductile deformation

All samples in this study are composed of coarser-grained porphyroclasts and finer-grained material (rock matrix). Thin sections were cut orthogonal to the foliation plane defined by alternating coarse- and fine-grained layers, which we interpret as the shear plane (Figs. 2a-c), and parallel to the lineation defined by the long axis of porphyroclasts. The rock matrix consists of bands of very fine-grained material that are oriented parallel to the interpreted shear plane (Figs. 2d-i), which we will refer to as shear bands. In higher strain samples (mylonites and ultramylonites), shear bands alternate with coarser-grained olivine-rich domains within the matrix. We classified samples as LT, MT, or HT based on the mineralogy of the shear bands, as these features developed during ductile deformation (Fig. 2).

Porphyroclasts of orthopyroxene (Opx1), clinopyroxene (Cpx1), and Al-Cr spinel (Spl1) are present in samples from all three categories. In protomylonitic samples, olivine (Ol1) is also present as porphyroclasts, but is only present in the matrix in mylonites and ultramylonites. In the two samples from dredge 19, plagioclase (Plg1) is present as coronas around Spl1.

LT mylonites are characterized by serpentine-rich bands oriented parallel to the shear plane (Fig. 2). The serpentine layers occasionally contain talc, chlorite, amphibole, and oxides, in textural equilibrium with serpentine (Fig. C.1). MT mylonites (Fig. 2e, h) are characterized by amphibole and chlorite aligned and elongated parallel to the shear plane. Amphibole-rich bands may be continuous on

199 the thin section scale, whereas chlorite is less abundant and dispersed, usually forming coronas around
200 Al-free Cr-spinel (Figs. 2e and h). HT mylonites (Fig. 2) contain amphibole in their shear bands (Fig.
201 2i), but otherwise have the standard anhydrous mineral assemblage of peridotites. In contrast to MT
202 mylonites, chlorite is absent in HT mylonites, and spinel is unaltered and Al-rich.

203 Grain size of serpentine and chlorite could not be determined microscopically. Other phases
204 located in shear bands have <20 µm mean grain sizes, with no clear relationship between shear band
205 grain size and rock texture. Shear bands in rocks with protomylonitic and ultramylonitic textures have
206 average grain sizes of 5-10 µm, while mylonitic textures seem to have slightly higher grain sizes, on
207 the order of 10-20 µm.

208

209 **4.2. Petrographic observations of brittle deformation**

210 All samples underwent brittle deformation in addition to ductile deformation, as evidenced by the
211 presence of crosscutting intra- and trans-granular fractures (Fig. 2). All three types of mylonites are
212 crosscut by serpentine ± magnetite ± talc filled fractures, which are classified as LT fractures based on
213 their mineral assemblage (Table 1). In addition, the MT and HT mylonites are crosscut by chlorite +
214 amphibole-filled fractures, which are classified as MT fractures (Table 1).

215 In addition to LT and MT fractures, we also identified HT fractures in the microstructures of
216 the HT mylonites. In these samples, porphyroclasts are often fractured and fragmented (Fig. 3). Many
217 of these fractured grains show evidence of intra-crystalline plasticity prior to fracturing, based on the
218 occurrence of grains that are elongated, bent, or have undulose extinction (Figs. 3a and c). These intra-
219 granular fractures are filled with the same mineral assemblage that is present in the shear bands in
220 these rocks (Figs. 3b and d): amphibole, sulfide, olivine, orthopyroxene (Opx2), clinopyroxene
221 (Cpx2), spinel (Spl2) ± plagioclase (Plg2). These minerals are also found to have similar chemical
222 compositions to minerals in the shear bands (Supplementary Table 2).

HT mylonites also contain fractures that crosscut the samples and are filled with amphibole ± sulfides (Fig. 2c). We refer to these as transgranular fractures, as they crosscut many grains without following grain boundaries. We observed them in the four HT samples that have mylonitic and ultramylonitic textures (Table 1), and in great number in mylonite PROT5-18-11. Interestingly, some of these HT transgranular fractures were subsequently offset by ductile deformation within shear bands (e.g., Fig. 4).

4.3. Amphibole composition

Amphibole is present in shear bands and fractures in all the mylonites and has a wide compositional range that reflects a range of formation conditions (Fig. 5). In HT mylonites, amphibole is pargasite or Mg-hornblende in composition and no intragranular zoning is observed (Fig. 5a). Amphibole composition varies between the proto- and ultra-mylonites (Fig. 5a), with the Si content of amphibole increasing with increasing intensity of deformation. However, amphibole composition does not vary between the fractures and the fine-grained ductile shear bands (Fig. 5a).

In MT mylonites, amphibole is Mg-hornblende to tremolite in composition (Fig. 5b) and has a Si content between 7.1 and 7.6 apfu. Only samples AII107-6-60-07 (Si, 6.7-6.8 apfu) and AII107-6-60-68 (Si, 7.8-7.9 apfu) fall outside this range (Fig. 5b). In both these samples, amphibole grains have concentric chemical zoning, with the cores having lower Si and higher alkali contents (Fig. 5b), as well as higher Al and Ti contents (Supplementary Table 2) than the rims. The transition from core to rim composition is sharp, occurring over a distance <3 μm (Fig. C.2). In AII107-6-60-07, cores and rims are both Mg-hornblende, but the core composition is similar to amphibole in HT mylonites, while the rim composition is similar to the majority of other MT mylonites (Figs. 5a-b). In AII107-6-60-68, cores are Mg-hornblende and rims are tremolite in composition (Fig. 5b).

Amphibole was only analyzed in one LT mylonite (sample AII107-6-61-89). This sample has two generations of amphibole: a first generation found in textural equilibrium with minerals in the coarser-grained olivine-rich zones of the matrix, and a second generation located in the shear bands in

textural equilibrium with serpentine (Fig. C.1). The first generation is of Mg-hornblende to tremolite composition (Si, 7.4-7.6 apfu; Fig. 5b). The second generation of amphibole, associated with LT deformation, is tremolite in composition and has Si contents of 7.9-8.0 apfu (Fig. 5b).

Amphiboles in LT to HT mylonites have chlorine concentrations ranging from below the detection limit up to 0.67 wt% (Fig. 5c). Chlorine shows an overall trend of decreasing concentration with increasing silica, i.e. from amphibole in HT to LT mylonites (Fig. 5c). In addition, chlorine decreases with increasing Fe#, $Fe^{2+}/(Fe^{2+}+Mg)$, (Fig. C.3). These variations are interpreted to reflect the structural control of Cl incorporation in amphibole (e.g., Campanaro and Jenkins, 2017). The overall amount of Cl in the amphiboles is relatively high, with up to 10^5 times the predicted concentration of Cl in the Depleted Mantle (Cl_{DM} = 0.14–0.38 μg/g; Urann et al., 2017).

4.4. P-T-fluid conditions during deformation

To evaluate the P-T conditions during mylonitic deformation, we used two empirical geothermometers that are based on the composition of orthopyroxene. Temperatures were calculated for porphyroclasts (cores and rims) for all categories of mylonites and for matrix shear bands in samples where orthopyroxene was found, totaling five HT and one MT samples (Table 2). Both $T_{Ca\text{-}in\text{-}Opx}$ and $T_{Al\text{-}Cr\ in\ Opx}$ thermometers indicate that, in each sample, porphyroclast cores have higher temperatures than porphyroclast rims, and that porphyroclast rim temperatures are systematically higher than matrix grain temperatures (Fig. 6a). The composition of grains located in HT shear bands imply higher temperatures than that of grains located in shear bands of the MT mylonite samples (Fig. 6a). Temperatures in HT mylonites range from 600 to 875°C with an average of ~700°C for $T_{Al\text{-}Cr\ in\ Opx}$, and range from 700 to 850°C with an average of ~760°C for $T_{Ca\text{-}in\text{-}Opx}$ (Fig. 6a). For the composition of 7 orthopyroxene grains found in the shear bands of one MT mylonite sample, both thermometers give an average temperature of ~600°C (Fig. 6a).

P-T pseudosections were built using Perple_X and provide constraints on the stability of phases associated with LT, MT and HT mylonite deformation. Fig. 6b shows the pseudosection of

sample PROT5-19-08 calculated under water-saturated conditions. We also calculated pseudosections for six other samples (Fig. B.1) and found that the compositional variations among peridotites in this study do not significantly influence the stability fields of the observed hydrous phases. The stability of hydrous phases (serpentine, talc, chlorite, pargasite/Mg-hornblende and tremolite) is mainly temperature-dependent and is only slightly sensitive to pressure (Fig. 6b). The presence of syn-deformational serpentine suggests that the LT mylonites formed at temperatures <500-650°C. This corresponds to the upper stability limit of antigorite and thus the highest temperature conditions at which any serpentine polymorph can be present (Guillot et al., 2015 and references therein). The presence of chlorite in MT mylonites constrains their deformation temperatures between 500 and 800°C. In HT mylonites, the only hydrous phase is pargasite to Mg-hornblende amphibole, which implies deformation at temperatures >750-800°C.

The pseudosection results agree well with the mineral thermometry estimate of ~600°C for the deformation temperature of matrix grains in MT mylonites (Fig. 6). For matrix grains in the HT mylonites, thermometry suggests a temperature range of 600-700 to 850-875°C (Fig. 6a). However, thermometric estimates below <750°C are not consistent with mylonite deformation under water-saturated conditions because chlorite is expected to form (Fig. 6b). These lower temperature estimates can be either explained by continued subsolidus diffusive re-equilibration of orthopyroxene compositions after deformation or by deformation of HT mylonites at water-undersaturated conditions (<0.5 wt%; Fig. B.2).

5. Discussion

Our petrological and geochemical observations indicate that peridotite mylonites and serpentinites dredged from the Shaka and Pr. Edward OTFs deformed by brittle and ductile processes within three distinct temperature ranges, forming LT (<500-650°C), MT (~500-800°C) and HT (>750-800°C) mylonites. The following discussion focuses first on the evidence for seawater-peridotite interaction during deformation from LT to HT conditions. We then use our microstructural and chemical analyses

of the mylonite to evaluate the depth extent and mechanism of seawater percolation and mantle hydration on OTF. Finally, we discuss the implications of fluid-mantle interaction for fault zone structure, rheology and geochemistry.

5.1. Seawater-mantle interaction from LT to HT conditions

Mylonites from the Shaka and Pr. Edward OTFs show evidence of interaction with seawater over a wide range of temperatures. The mylonite protolith is assumed to have been typical coarse-grained upper mantle peridotite, which does not contain hydrous phases (e.g., Dick et al., 1984; Warren, 2016). The absence of porphyroclasts of hydrous phases also suggests that no hydrous phase was present in the protolith prior to deformation. In contrast, hydrous phases are systematically present, and commonly abundant, in the shear bands of the mylonites, indicating that they crystallized during mylonite formation (Fig. 2). Serpentine (± talc, chlorite, amphibole) formed at LT conditions, chlorite and amphibole at MT conditions, and amphibole at HT conditions. Amphibole is present in LT to HT mylonites and has high concentrations of chlorine (Fig. 5c), which in HT mylonites is up to 10^5 times the predicted concentration of the upper mantle (Urann et al., 2017). At lower temperature, amphibole contains less chlorine due to structural controls of Cl incorporation in amphibole (e.g., Campanaro and Jenkins, 2017). The abundance of chlorine in amphibole and the overall abundance of hydrous minerals suggest that hydrous minerals formed within the shear bands formed as a result of syn-deformational interaction of peridotite with seawater.

The continuous spectrum of amphibole compositions suggests that mylonite formation and mantle hydration occurred over a continuous temperature range from LT to HT conditions. Experiments have shown that the Si content of amphibole in peridotites is inversely proportional to its crystallization temperature (Fumagalli et al., 2009). The continuous decrease in Si from HT pargasite to LT tremolite (Fig. 5) is therefore consistent with continuous amphibole crystallization and mantle-fluid interaction from LT to HT conditions. Some amphiboles have sharp zoning, with cores and rims having distinct compositions (Fig. B.1), which suggests that some rocks underwent two separate

episodes of fluid/rock interaction during deformation, at two distinct temperatures during rock cooling and uplift to the seafloor.

Our thermometry estimates argue for formation of HT mylonites, and therefore seawater-mantle interaction, at temperatures >850-875°C. The maximum temperature calculated for minerals in HT shear bands using the $T_{Ca\ in\ Opx}$ and the $T_{Al\text{-}Cr\ in\ Opx}$ thermometers is 850°C and 875°C, respectively (Fig. 6a). In each sample, the estimated deformation temperatures of matrix grains are lower than those estimated for both the cores and rims of porphyroclasts (Table 2). This suggests that orthopyroxene matrix grains chemically (re)equilibrated during deformation and thus provide information on the temperature of HT mylonite deformation. Linckens et al. (2011) used 1D diffusion modelling to estimate a closure temperature of ~800°C for orthopyroxene major element-based thermometers for a grain size of 50 µm. Hence, our estimates of 850-875°C are above the closure temperature of the two thermometers and thus represent minimum estimates of the maximum temperature of HT mylonite deformation.

Our results support seawater percolation and continuous fluid-mantle interaction up to high temperature conditions on transform faults. Analysis of rock samples from the Vema OTF on the MAR (Fig. 1f) supports our interpretations as serpentinite (LT), amphibole-chlorite (MT) and amphibole-bearing (HT) mylonites have also been dredged in large proportions on the Vema southern transform valley walls (Cannat et al., 1991; Cannat and Seyler, 1995; Cipriani et al., 2009). Amphibole in the Vema samples has similar compositions (Cipriani et al., 2009) to SWIR mylonite amphiboles, suggesting a similar temperature range for fluid-mantle interaction. Overall, observations of mylonites from OTFs indicate that hydrothermal fluids interact with the mantle up to at least 850-875°C and that this might be a common process on OTFs.

5.2. Depth of seawater percolation and mylonite formation

The depth of LT, MT and HT mylonite deformation cannot be directly estimated from our samples, as hydrous mineral stability in peridotites is mainly temperature-dependent (Fig. 6b), and mineral-based

353 empirical barometers are not available for spinel-bearing peridotites. Therefore, to convert temperature
354 constraints to depth, we use numerical models of fault thermal structure for the Shaka and Pr. Edward
355 OTFs (Fig. 7a).

356 To evaluate the thermal structure of these two SWIR OTFs, we first use the results of a 3D visco-
357 plastic, thermomechanical model (e.g., Behn et al., 2007; Roland et al., 2010) of Shaka OTF. The
358 model is composed of two ridge segments offset by a transform fault. Three-dimensional mantle flow
359 is driven kinematically by imposing a half-slip rate on either side of the transform fault at the surface
360 of the model. As Shaka and Pr. Edward faults have similar slip rates and offsets and neither are
361 segmented (e.g., Wolfson-Schwehr and Boettcher, 2019), we consider their thermal structures to be
362 similar (Fig. 7a) and calculate the Pr. Edward thermal structure from the scaling relations developed
363 by Wolfson-Schwehr et al. (2017) based on fault slip rate. The full slip rates of the two faults are from
364 the NUVEL-1 model (Argus and Gordon, 1991) and fault lengths are from the database of Wolfson-
365 Schwehr and Boettcher (2019).

366 Based on the thermal models of the two OTFs, serpentinization and LT deformation occurs up to
367 temperatures of 500-550°C, which corresponds to depths of ~11-13 km in the thermal model. LT
368 mylonites formed somewhere within this domain and characterization of the serpentine polymorph
369 (antigorite versus lizardite and/or chrysotile) could provide more specific constraints on the
370 temperature of formation (e.g., Guillot et al. 2015). MT mylonite formation occurs at up to 700-
371 750°C (16-19 km). Finally, our maximum estimate of >850-875°C for HT mylonite formation, and the
372 limit of mantle hydration on OTFs, corresponds to depths >22-25 km. All together, these results prove
373 that seawater can percolate deep into OTFs.
374

375 **5.3. Fracturing as a mechanism for deep hydrothermal fluid percolation**

376 Our results highlight seawater percolation and mantle hydration up to at least 850-875°C on OTFs. As
377 discussed in Kohli and Warren (In Press), this observation contradicts the traditional view of the
378 600°C isotherm as the limit of brittle behavior in the oceanic lithosphere (Abercrombie and Ekström,
379 2001; Boettcher et al., 2007; Jaroslow et al., 1996; McKenzie et al., 2005), and thereby the limit of

seawater percolation on OTFs (e.g., Sibson et al., 1975). In contrast, we show direct evidence of brittle deformation of peridotites at higher temperature, which is consistent with observations of deep earthquakes from recent seismic surveys (Kuna et al., 2019; McGuire et al., 2012; Wolfson-Schwehr et al., 2014).

Our microstructural observations of HT mylonites reveal HT fracturing events coeval with mylonitic ductile deformation (Figs. 3 and 4). In every sample, porphyroclasts can be crosscut by fractures (Fig. 3). These fractures are filled with the same mineral assemblage as observed in the mylonitic shear bands (Fig. 3) and show similar chemical compositions (e.g., Fig. 5a),. This high temperature semi-brittle behavior is also shown by the offset of amphibole-filled transgranular veins by HT shear bands in HT mylonites and ultramylonites (Fig. 4). This provides additional support for the idea that fractures developed during ductile deformation within the shear bands.

We propose that this HT fracturing process was the driving force for the deep downward migration of hydrothermal fluids, which resulted in HT mylonite hydration. Our results show that amphibole systematically occurs in the sealing material of porphyroclast fractures (Fig. 3) and is the dominant phase sealing transgranular fractures (Fig. 2i). This indicates that, at the sample scale, brittle failure locally enhanced rock permeability, driving fluid flow and amphibole crystallization in HT mylonites. Accordingly, we propose that this HT brittle behavior of peridotites leads to the formation of hydrothermal fluid pathways, allowing for deep seawater percolation and mantle hydration within the fault zone (Fig. 7b). In HT and MT mylonites, amphibole is concentrated in fine-grained shear zones and absent from coarser-grained zones (Figs. 2h and i; Kohli et al, in press). This might suggest that, after fracturing and fluid flow, subsequent ductile deformation is localized and possibly drives fluid flow preferentially through mylonitic regions (Fusseis et al., 2009; Précigout et al., 2017).

Brittle behavior of peridotites in fault zones is thought to be limited to ~600°C, which corresponds to the temperature of the brittle-ductile transition of olivine at tectonic strain rates (10^{-12}-10^{-15} s^{-1}). This temperature was determined by extrapolating the results of deformation experiments on olivine aggregates from laboratory strain rates (10^{-4}-10^{-7} s^{-1}) to tectonic strain rates (Boettcher et al.,

406 2007). Here, we provide evidence for brittle behavior of mantle peridotites at much higher
407 temperatures. This suggests that the mechanism for HT fracturing of the coarse-grained peridotite
408 protolith is deformation at strain rates higher than tectonic strain rates. The experiments of Boettcher
409 et al. (2007) show that brittle deformation in olivine at temperatures up to ~900°C requires strain rates
410 of 10^{-8} s^{-1} or higher, which is consistent with estimates from Kohli and Warren (2019) based on
411 rheological modeling of the Shaka mylonites.

412 Our observations of high temperature brittle failure in the mylonites agrees with the results of
413 two recent ocean bottom seismometer campaigns on the Gofar and Discovery OTFs on the fast
414 slipping East Pacific Rise (McGuire et al., 2012; Wolfson-Schwehr et al., 2014) and on the Blanco
415 OTF on the intermediate slipping Juan de Fuca Ridge (Kuna et al., 2019). Based on similar thermal
416 models as in Fig. 7, earthquakes located within the mantle imply brittle failure above 600°C on both
417 faults, and possibly up to 1000-1100°C on Gofar (Guo et al., 2018; Roland et al., 2012). Brittle
418 deformation of mantle peridotites at temperatures above their long-term brittle-ductile transition
419 therefore seems to characteristic of both fast- to ultraslow slipping OTFs, from, which suggests that
420 deep seawater percolation exists across the global transform system.
421

422 **5.4. Evolution of fault zone structure and slip behavior due to fluid-rock interaction**

423 In the ocean bottom seismometer campaigns, spatial variations have been observed in the seismic
424 behavior of the mantle. The mantle at temperatures below 600°C deforms by aseismic creep or can
425 slip seismically in either large, quasi-periodic mainshocks or micro-earthquakes (Kuna et al., 2019).
426 Above the 600°C isotherm, the mantle deforms aseismically in some sections of the faults, while
427 micro-earthquakes are recorded on other sections (Guo et al., 2018; Kuna et al., 2019; Roland et al.,
428 2012). Some of these variations may be explained by spatial variations in the intensity of mantle
429 deformation and hydration.

430 An important implication of the fluid-mantle interaction recorded in mylonites from the Shaka
431 and Pr. Edward OTFs is that the structure and the rheology of the mantle evolves as a function of time,
432 strain and hydration. With increasing intensity of peridotite deformation and hydration, mantle

433 deformation transitions from being accommodated by deformation of dry, coarse-grained peridotites,
434 mainly olivine, to being controlled by the rheology of interconnected, weak LT, MT and HT mylonitic
435 shear zones (Fig. 7b).

436 In the LT domain, progressive accommodation of fault slip by serpentinite shear zones on
437 active OTFs is consistent with observations of the exhumed Southern Troodos Transform Fault Zone
438 (Cyprus). Studies have highlighted that the dominant structures in the mantle section of this ~5 km
439 wide fault zone are serpentinite mélange (MacLeod and Murton, 1995), with the proportion of
440 serpentinite matrix to embedded blocs increasing with strain (Fagereng and MacLeod, 2019).
441 Serpentine is a mechanically weak mineral and, in contrast to olivine, can steadily creep at tectonic
442 strain rates and LT temperature conditions (Guillot et al., 2015 and references therein). These
443 observations recently lead Fagereng and MacLeod (2019) to propose that spatio-temporal variations in
444 mantle serpentinization could explain lateral variations observed in the seismic behavior of OTFs at
445 temperatures less than 600°C (e.g., Wolfson-Schwehr and Boettcher, 2019). Serpentinized segments of
446 the fault zone would have low seismic coupling and would creep aseismically, whereas segments
447 composed of dry peridotites would be locked interseismically between seismic events.

448 Deeper on the OTFs, deformation in hydrated shear zones is mainly accommodated by chlorite
449 and amphibole assemblages at MT conditions (Fig. 2h) and by fine-grained, amphibole-bearing
450 assemblages at HT conditions (Fig. 2i). The mechanical behavior of such assemblages has not been
451 studied experimentally. We know, however, that chlorite is a mechanically weak phyllosilicate owing
452 to its planar crystallographic structure, and the presence of chlorite can therefore trigger peridotite
453 weakening (e.g., Amiguet et al., 2012). In contrast, Tommasi et al. (2017) found no evidence of
454 peridotite weakening associated with increasing amounts of amphibole in a study of a natural upper
455 mantle shear zone containing pargasitic amphibole. However, this result may not be applicable the MT
456 mylonites where tremolitic amphibole forms continuous bands at the sample scale. In addition, Kohli
457 and Warren (In Press) found that the presence of amphibole promoted olivine grain size reduction and
458 thus weakening through a transition from grain-size insensitive to grain-size sensitive creep. In this
459 study, we also found that the grain size reduction associated with both MT and HT mylonite

deformation provides a weakening mechanism. Kohli et al. (subm.) also noted that this switch causes a shallowing of the brittle-ductile transition in the mantle lithosphere. Variations in the depth extent of microseismicity in the mantle on OTFs (Guo et al., 2018; Kuna et al., 2019; McGuire et al., 2012; Roland et al., 2012) could therefore be explained by variations in the degree of strain and hydration within the fault zones, with aseismic (ductile) zones being more deformed and hydrated than seismic (brittle) patches.

We conclude that increasing hydration and strain of mantle rocks on OTFs leads to weakening from LT to HT conditions and changes in seismic behavior. Lateral variations in mantle seismicity may thus be explained by lateral variations in the intensity of mantle deformation and fluid-rock interaction.

5.5. Implications of deep fluid-rock interaction for volatile cycling and subduction zone dynamics

Oceanic fracture zones (OFZs) are the relict trace of OTFs that extend beyond mid-ocean ridge offsets and eventually enter the mantle at subduction zones (e.g., Manea et al., 2014). The depth and extent of hydration of the lithosphere at OTFs is therefore important to the global volatile cycle and the geochemical budget of subduction zones. Phases precipitating after hydrothermal fluid-mantle interaction, especially serpentine, chlorite and amphibole, are able to host large amounts of volatiles in their mineral structures. This includes water (~13 wt% for serpentine; e.g., Ulmer and Trommsdorff, 1995) and fluid-mobile elements such as boron, chlorine, strontium (e.g., Scambelluri et al., 2004; Urann et al., 2017). Our observations of deep and intense mantle hydration on OTFs indicate a depth range of 11-13 km for serpentinization on ultra-slow slipping OTFs, which has important implications for subduction. At slab de-serpentinization temperatures (~600-700°C; e.g., Ulmer and Trommsdorff, 1995), higher water flux into the overlying mantle wedge would be promoted in regions of subducting OFZs compared to the surrounding oceanic lithosphere. This could explain the overall higher rate of seismicity (Schlaphorst et al., 2016) and clustering of deep intra-slab seismicity (Paulatto et al., 2017)

observed in sub-arc regions along the Lesser Antilles subduction zone where several MAR OFZs are subducting.

In addition to water, modeling results of McCaig et al. (2018) suggest that the process of deep and intense hydrothermal fluid flow on OTFs, as we observe in this study, is needed to add significant boron to the mantle. On fault systems which are not long-lived and/or permeable (e.g., bending faults found in the outer rise of subduction zones), boron is completely consumed through crustal alteration before hydrothermal fluids reach the mantle. Deep fluid flow and mantle serpentinization on OTFs, as well as deserpentinization at sub-arc depths, therefore could account for the observation that volcanoes located above subducting OFZs along the Aleutian and Andean margins have lavas relatively enriched in boron compared to other arc volcanoes (Manea et al., 2014).

6. Conclusion

Our study of deformed peridotites and serpentinites dredged from the Shaka and Pr. Edward OTFs indicate deep and intense fluid-rock interaction during deformation of peridotites on OTFs. By combining observations of the mineral assemblages present in fractures and shear bands with thermometric and thermodynamic calculations, we identified three domains of deformation corresponding to different temperature conditions. They are characterized by crystallization of (i) serpentine (± talc ± tremolitic amphibole ± chlorite ± oxides) at <500-550°C (LT domain), (ii) chlorite, Mg-hornblende to tremolitic amphibole and oxides at ~500-750°C (MT domain), and (iii) pargasitic to Mg-hornblende amphibole, sulfides and new peridotitic minerals at >750°C (HT domain). The crystallization of Cl-rich amphibole in each domain indicates that the peridotite reacted with seawater-derived fluids during deformation.

In each domain, samples record evidence of deformation by both brittle and ductile mechanisms, with fracturing and fluid-mantle interaction leading to the progressive formation of LT, MT and HT mylonites. Empirical thermometers indicate HT semi-brittle deformation and mantle hydration extended to temperatures up to at least 850-875°C, beyond the long-term brittle-ductile

transition of olivine, and likely results from high strain rates in the fault zones. We applied our temperature constraints on the mylonites to modeled geotherms of Shaka and Pr. Edward OTFs, which indicates that mantle serpentinization extends to ~11-13 km and deep seawater percolation extends to ~25-30 km.

The evolution in fault zone structure induced by progressive fracturing and fluid-rock interaction leads to the crystallization of weak phases at shallow levels and grain size reduction deeper on the fault, providing mechanisms to account for weakening and strain localization processes within the hydrated portions of the mantle on OTFs. Due to intense and deep fluid-rock interaction, the mantle lithosphere on OTFs also likely represents very large reservoirs for volatiles and are thus important elements of the Earth's volatile cycle.

Acknowledgments

We are grateful to Anette van der Handt, Valentina Batanova and Valérie Magnin for their technical support and advice on EPMA analyses and to Yong Zhao for assistance with the University of Delaware SEM. This work was supported by National Science Foundation grants EAR-1347696 and EAR-1619880, and funds provided to Jessica Warren as part of the University Startup funding.

References

Abercrombie, R.E., Ekström, G., 2001. Earthquake slip on oceanic transform faults. Nature 410, 74–77.

Amiguet, E., Reynard, B., Caracas, R., Van de Moortèle, B., Hilairet, N., Wang, Y., 2012. Creep of phyllosilicates at the onset of plate tectonics. Earth Planet. Sci. Lett. 345, 142–150.

Argus, D.F., Gordon, R.G., 1991. No-net-rotation model of current plate velocities incorporating plate motion model NUVEL-1. Geophys. Res. Lett. 18, 2039–2042.

Armstrong, J.T., 1988. Quantitative analysis of silicate and oxide minerals: comparison of Monte Carlo, ZAF and phi-rho-z procedures. Microbeam Anal. 23, 239–246.

Batanova, V.G., Sobolev, A.V., Kuzmin, D.V., 2015. Trace element analysis of olivine: High precision analytical method for JEOL JXA-8230 electron probe microanalyser. Chem. Geol. 419, 149–157.

Behn, M.D., Boettcher, M.S., Hirth, G., 2007. Thermal structure of oceanic transform faults. Geology 35, 307–310.

Boettcher, M.S., Hirth, G., Evans, B., 2007. Olivine friction at the base of oceanic seismogenic zones. J. Geophys. Res. Solid Earth 112.
Boschi, C., Bonatti, E., Ligi, M., Brunelli, D., Cipriani, A., Dallai, L., D'Orazio, M., Früh-Green, G.L., Tonarini, S., Barnes, J.D., 2013. Serpentinization of mantle peridotites along an uplifted lithospheric section, Mid Atlantic Ridge at 11 N. Lithos 178, 3–23.
Brey, G.P., Köhler, T., 1990. Geothermobarometry in four-phase lherzolites II. New thermobarometers, and practical assessment of existing thermobarometers. J. Petrol. 31, 1353–1378.
Caine, J.S., Evans, J.P., Forster, C.B., 1996. Fault zone architecture and permeability structure. Geology 24, 1025–1028.
Campanaro, B.P., Jenkins, D.M., 2017. An experimental study of chlorine incorporation in amphibole synthesized along the pargasite–ferro-pargasite join. Can. Mineral. 55, 419–436.
Cannat, M., Mamaloukas-Frangoulis, V., Auzende, J.-M., Bideau, D., Bonatti, E., Honnorez, J., Lagabrielle, Y., Malavieille, J., Mevel, C., 1991. A geological cross-section of the Vema fracture zone transverse ridge, Atlantic ocean. J. Geodyn., Symposium Sy19- European Union of Geosciences Meeting 13, 97–117. https://doi.org/10.1016/0264-3707(91)90034-C
Cannat, M., Seyler, M., 1995. Transform tectonics, metamorphic plagioclase and amphibolitization in ultramafic rocks of the Vema transform fault (Atlantic Ocean). Earth Planet. Sci. Lett. 133, 283–298. https://doi.org/10.1016/0012-821X(95)00078-Q
Chantler, C.T., Olsen, K., Dragoset, R.A., Kishore, A.R., Kotochigova, S.A., Zucker, D.S., 2005. X-ray form factor, attenuation and scattering tables (version 2.1) National Institute of Standards and Technology. Gaithersburg MD Available Httpphysics Nist Govffast.
Cipriani, A., Bonatti, E., Seyler, M., Brueckner, H.K., Brunelli, D., Dallai, L., Hemming, S.R., Ligi, M., Ottolini, L., Turrin, B.D., 2009. A 19 to 17 Ma amagmatic extension event at the Mid-Atlantic Ridge: Ultramafic mylonites from the Vema Lithospheric Section 10, 1–53. https://doi.org/10.7916/D8V69V86
Connolly, J. a. D., 2009. The geodynamic equation of state: What and how. Geochem. Geophys. Geosystems 10. https://doi.org/10.1029/2009GC002540
Dick, H.J., Fisher, R.L., Bryan, W.B., 1984. Mineralogic variability of the uppermost mantle along mid-ocean ridges. Earth Planet. Sci. Lett. 69, 88–106.
Donovan, J.J., Singer, J.W., Armstrong, J.T., 2016. A new EPMA method for fast trace element analysis in simple matrices. Am. Mineral. 101, 1839–1853.
Fagereng, \AAke, MacLeod, C.J., 2019. On Seismicity and Structural Style of Oceanic Transform Faults: A Field Geological Perspective From the Troodos Ophiolite, Cyprus, in: Transform Plate Boundaries and Fracture Zones. Elsevier, pp. 437–459.
Farmer, H.G., Dick, H.J., 1981. Description of WHOI rock dredge samples: volume 3. Woods Hole Oceanographic Institution.
Faulkner, D.R., Jackson, C.A.L., Lunn, R.J., Schlische, R.W., Shipton, Z.K., Wibberley, C.A.J., Withjack, M.O., 2010. A review of recent developments concerning the structure, mechanics and fluid flow properties of fault zones. J. Struct. Geol. 32, 1557–1575.
Fisher, R.L., Dick, H.J.B., Natland, J.H., Meyer, P.S., 1986. Mafic/Ultramafic Suites of the Slowly Spreading Southwest Indian Ridge: Protea Exploration of the Antarctic Plate Boundary, 24E-47E. Ofioliti 11, 147–178.
Fisher, R.L., Natland, J.H., Dick, H.J.B., 1985. Mafic and ultramafic rock assemblages from the Antarctic Plate boundary, southwest Indian Ocean. Antarct. J. Rev. 94–96.
Froment, B., McGuire, J.J., van der Hilst, R.D., Gouédard, P., Roland, E.C., Zhang, H., Collins, J.A., 2014. Imaging along-strike variations in mechanical properties of the Gofar transform fault, East Pacific Rise. J. Geophys. Res. Solid Earth 119, 7175–7194. https://doi.org/10.1002/2014JB011270
Fumagalli, P., Zanchetta, S., Poli, S., 2009. Alkali in phlogopite and amphibole and their effects on phase relations in metasomatized peridotites: a high-pressure study. Contrib. Mineral. Petrol. 158, 723–737. https://doi.org/10.1007/s00410-009-0407-4

595 Fusseis, F., Regenauer-Lieb, K., Liu, J., Hough, R.M., De Carlo, F., 2009. Creep cavitation can establish
596 a dynamic granular fluid pump in ductile shear zones. Nature 459, 974–977.
597 https://doi.org/10.1038/nature08051
598 Gregg, P.M., Lin, J., Behn, M.D., Montési, L.G., 2007. Spreading rate dependence of gravity anomalies
599 along oceanic transform faults. Nature 448, 183.
600 Guillot, S., Schwartz, S., Reynard, B., Agard, P., Prigent, C., 2015. Tectonic significance of
601 serpentinites. Tectonophysics 646, 1–19. https://doi.org/10.1016/j.tecto.2015.01.020
602 Guo, H., Zhang, H., Froment, B., 2018. Structural control on earthquake behaviors revealed by high-
603 resolution Vp/Vs imaging along the Gofar transform fault, East Pacific Rise. Earth Planet. Sci.
604 Lett. 499, 243–255.
605 Hacker, B.R., Abers, G.A., Peacock, S.M., 2003. Subduction factory 1. Theoretical mineralogy,
606 densities, seismic wave speeds, and H2O contents. J. Geophys. Res. Solid Earth 108.
607 https://doi.org/10.1029/2001JB001127
608 Hansen, L.N., Cheadle, M.J., John, B.E., Swapp, S.M., Dick, H.J.B., Tucholke, B.E., Tivey, M.A., 2013.
609 Mylonitic deformation at the Kane oceanic core complex: Implications for the rheological
610 behavior of oceanic detachment faults: Rheology of Kane Oceanic Core Complex. Geochem.
611 Geophys. Geosystems 14, 3085–3108. https://doi.org/10.1002/ggge.20184
612 Jaroslow, G.E., Hirth, G., Dick, H.J.B., 1996. Abyssal peridotite mylonites: implications for grain-size
613 sensitive flow and strain localization in the oceanic lithosphere. Tectonophysics 256, 17–37.
614 Kohli, A.H., Warren, J.M., 2019. Evidence for a deep hydrologic cycle on oceanic transform faults. J.
615 Geophys. Res. Solid Earth.
616 Kuna, V.M., Nábelek, J.L., Braunmiller, J., 2019. Mode of slip and crust-mantle interaction at oceanic
617 transform faults. Nat. Geosci. 1.
618 Linckens, J., Herwegh, M., Müntener, O., 2011. Linking temperature estimates and microstructures in
619 deformed polymineralic mantle rocks. Geochem. Geophys. Geosystems 12, Q08004.
620 https://doi.org/10.1029/2011GC003536
621 Locock, A.J., 2014. An Excel spreadsheet to classify chemical analyses of amphiboles following the
622 IMA 2012 recommendations. Comput. Geosci. 62, 1–11.
623 MacLeod, C.J., Murton, B.J., 1995. On the sense of slip of the Southern Troodos transform fault zone,
624 Cyprus. Geology 23, 257–260.
625 Manea, V.C., Leeman, W.P., Gerya, T., Manea, M., Zhu, G., 2014. Subduction of fracture zones
626 controls mantle melting and geochemical signature above slabs. Nat. Commun. 5, 5095.
627 McCaig, A.M., 1988. Deep fluid circulation in fault zones. Geology 16, 867–870.
628 McCaig, A.M., Delacour, A., Fallick, A.E., Castelain, T., Früh-Green, G.L., 2010. Detachment fault
629 control on hydrothermal circulation systems: Interpreting the subsurface beneath the TAG
630 hydrothermal field using the isotopic and geological evolution of oceanic core complexes in
631 the Atlantic, in: Rona, P.A., Devey, C.W., Dyment, J., Murton, B.J. (Eds.), Geophysical
632 Monograph Series. American Geophysical Union, Washington, D. C., pp. 207–239.
633 https://doi.org/10.1029/2008GM000729
634 McCaig, A.M., Titarenko, S.S., Savov, I.P., Cliff, R.A., Banks, D., Boyce, A., Agostini, S., 2018. No
635 significant boron in the hydrated mantle of most subducting slabs. Nat. Commun. 9.
636 McGuire, J.J., Collins, J.A., Gouédard, P., Roland, E., Lizarralde, D., Boettcher, M.S., Behn, M.D., Van
637 Der Hilst, R.D., 2012. Variations in earthquake rupture properties along the Gofar transform
638 fault, East Pacific Rise. Nat. Geosci. 5, 336.
639 McKenzie, D., Jackson, J., Priestley, K., 2005. Thermal structure of oceanic and continental
640 lithosphere. Earth Planet. Sci. Lett. 233, 337–349.
641 Miranda, E.A., John, B.E., 2010. Strain localization along the Atlantis Bank oceanic detachment fault
642 system, Southwest Indian Ridge. Geochem. Geophys. Geosystems 11.
643 Passchier, C.W., Trouw, R.A., 2005. Microtectonics. Springer Science & Business Media.
644 Paulatto, M., Laigle, M., Galve, A., Charvis, P., Sapin, M., Bayrakci, G., Evain, M., Kopp, H., 2017.
645 Dehydration of subducting slow-spread oceanic lithosphere in the Lesser Antilles. Nat.
646 Commun. 8, 15980.

Picazo, S., Cannat, M., Delacour, A., Escartín, J., Rouméjon, S., Silantyev, S., 2012. Deformation associated with the denudation of mantle-derived rocks at the Mid-Atlantic Ridge 13°–15° N: The role of magmatic injections and hydrothermal alteration. Geochem. Geophys. Geosystems 13.

Pickle, R.C., Forsyth, D.W., Harmon, N., Nagle, A.N., Saal, A., 2009. Thermo-mechanical control of axial topography of intra-transform spreading centers. Earth Planet. Sci. Lett. 284, 343–351. https://doi.org/10.1016/j.epsl.2009.05.004

Roland, E., Behn, M.D., Hirth, G., 2010. Thermal-mechanical behavior of oceanic transform faults: Implications for the spatial distribution of seismicity. Geochem. Geophys. Geosystems 11. https://doi.org/10.1029/2010GC003034

Roland, E., Lizarralde, D., McGuire, J.J., Collins, J.A., 2012. Seismic velocity constraints on the material properties that control earthquake behavior at the Quebrada-Discovery-Gofar transform faults, East Pacific Rise. J. Geophys. Res. Solid Earth 117.

Rouméjon, S., Cannat, M., 2014. Serpentinization of mantle-derived peridotites at mid-ocean ridges: Mesh texture development in the context of tectonic exhumation. Geochem. Geophys. Geosystems 15, 2354–2379. https://doi.org/10.1002/2013GC005148

Rüpke, L., Morgan, J.P., Hort, M., Connolly, J.A.D., 2004. Serpentine and the subduction zone water cycle. Earth Planet. Sci. Lett. 223, 17–34. https://doi.org/10.1016/j.epsl.2004.04.018

Scambelluri, M., Fiebig, J., Malaspina, N., Müntener, O., Pettke, T., 2004. Serpentinite subduction: implications for fluid processes and trace-element recycling. Int. Geol. Rev. 46, 595–613.

Schlaphorst, D., Kendall, J.-M., Collier, J.S., Verdon, J.P., Blundy, J., Baptie, B., Latchman, J.L., Massin, F., Bouin, M.-P., 2016. Water, oceanic fracture zones and the lubrication of subducting plate boundaries—insights from seismicity. Geophys. J. Int. 204, 1405–1420.

Scripps Institution of Oceanography, 1984. Shipboard description and inventory of rocks dredged on PROTEA expedition, R/V Melville, 14 January-15 February 1984, SIO reference. La Jolla, Calif: Scripps Institution of Oceanography, University of California, San Diego.

Sibson, R.H., Moore, J.M.M., Rankin, A.H., 1975. Seismic pumping—a hydrothermal fluid transport mechanism. J. Geol. Soc. 131, 653–659.

Sobolev, A.V., Hofmann, A.W., Kuzmin, D.V., Yaxley, G.M., Arndt, N.T., Chung, S.-L., Danyushevsky, L.V., Elliott, T., Frey, F.A., Garcia, M.O., others, 2007. The amount of recycled crust in sources of mantle-derived melts. Science 316, 412–417.

Tommasi, A., Langone, A., Padrón-Navarta, J.A., Zanetti, A., Vauchez, A., 2017. Hydrous melts weaken the mantle, crystallization of pargasite and phlogopite does not: Insights from a petrostructural study of the Finero peridotites, southern Alps. Earth Planet. Sci. Lett. 477, 59–72.

Ulmer, P., Trommsdorff, V., 1995. Serpentine stability to mantle depths and subduction-related magmatism. Science 268, 858–861.

Urann, B.M., Le Roux, V., Hammond, K., Marschall, H.R., Lee, C.-T., Monteleone, B.D., 2017. Fluorine and chlorine in mantle minerals and the halogen budget of the Earth's mantle. Contrib. Mineral. Petrol. 172, 51.

Warren, J.M., 2016. Global variations in abyssal peridotite compositions. Lithos 248, 193–219.

Witt-Eickschen, G., Seck, H.A., 1991. Solubility of Ca and Al in orthopyroxene from spinel peridotite: an improved version of an empirical geothermometer. Contrib. Mineral. Petrol. 106, 431–439.

Wolfson-Schwehr, M., Boettcher, M.S., 2019. Global Characteristics of Oceanic Transform Fault Structure and Seismicity, in: Transform Plate Boundaries and Fracture Zones. Elsevier, pp. 21–59.

Wolfson-Schwehr, M., Boettcher, M.S., Behn, M.D., 2017. Thermal segmentation of mid-ocean ridge-transform faults. Geochem. Geophys. Geosystems 18, 3405–3418.

Wolfson-Schwehr, M., Boettcher, M.S., McGuire, J.J., Collins, J.A., 2014. The relationship between seismicity and fault structure on the Discovery transform fault, East Pacific Rise. Geochem. Geophys. Geosystems 15, 3698–3712. https://doi.org/10.1002/2014GC005445

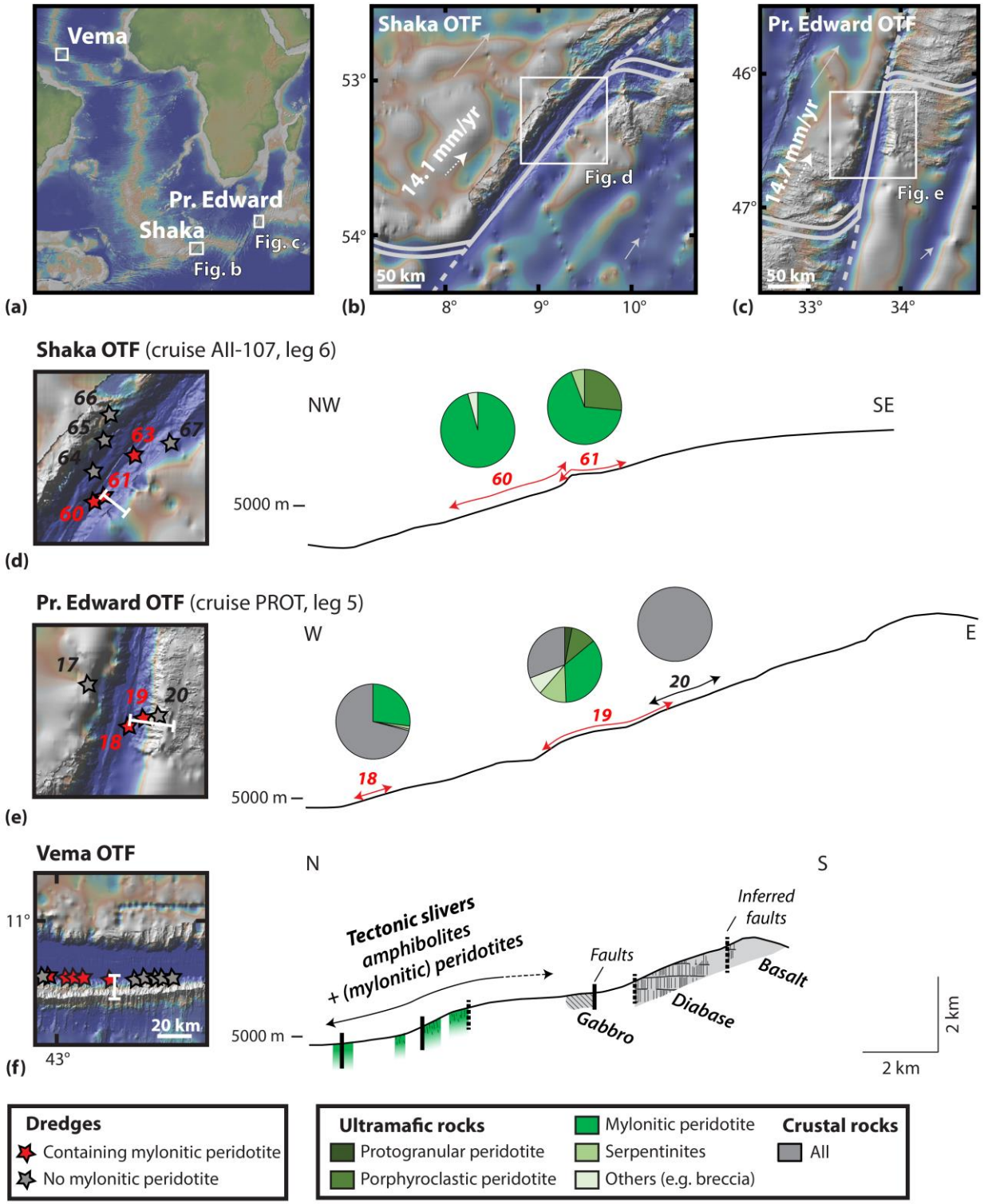

Fig. 1. Location (a) and bathymetric maps of the Shaka (b) and Pr. Edward (c) OTFs. (d-e) Map enlargements (left) and bathymetric profiles (right) of the Shaka and Pr. Edward OTFs. (f) Bathymetric map (left), geological cross-section (right) of the Vema OTF. The cross-section is adapted from Cannat et al. (1991) based on observations from dives 1 and 5. For all OTFs, the

transects are shown by white lines on the bathymetric maps, which show the location of dredges that either recovered (red stars) or did not recover (grey stars) peridotite mylonites. Bathymetric maps and profiles were constructed using GeoMapApp (Ryan et al., 2009). For the Shaka and Pr. Edward OTFs, dredge numbers are shown on the enlarged maps and nearby dredge compositions are shown on the profiles. For Vema OTF, dredge locations and compositions are from Cannat et al. (1991), Cipriani et al. (2009) and Boschi et al. (2013).

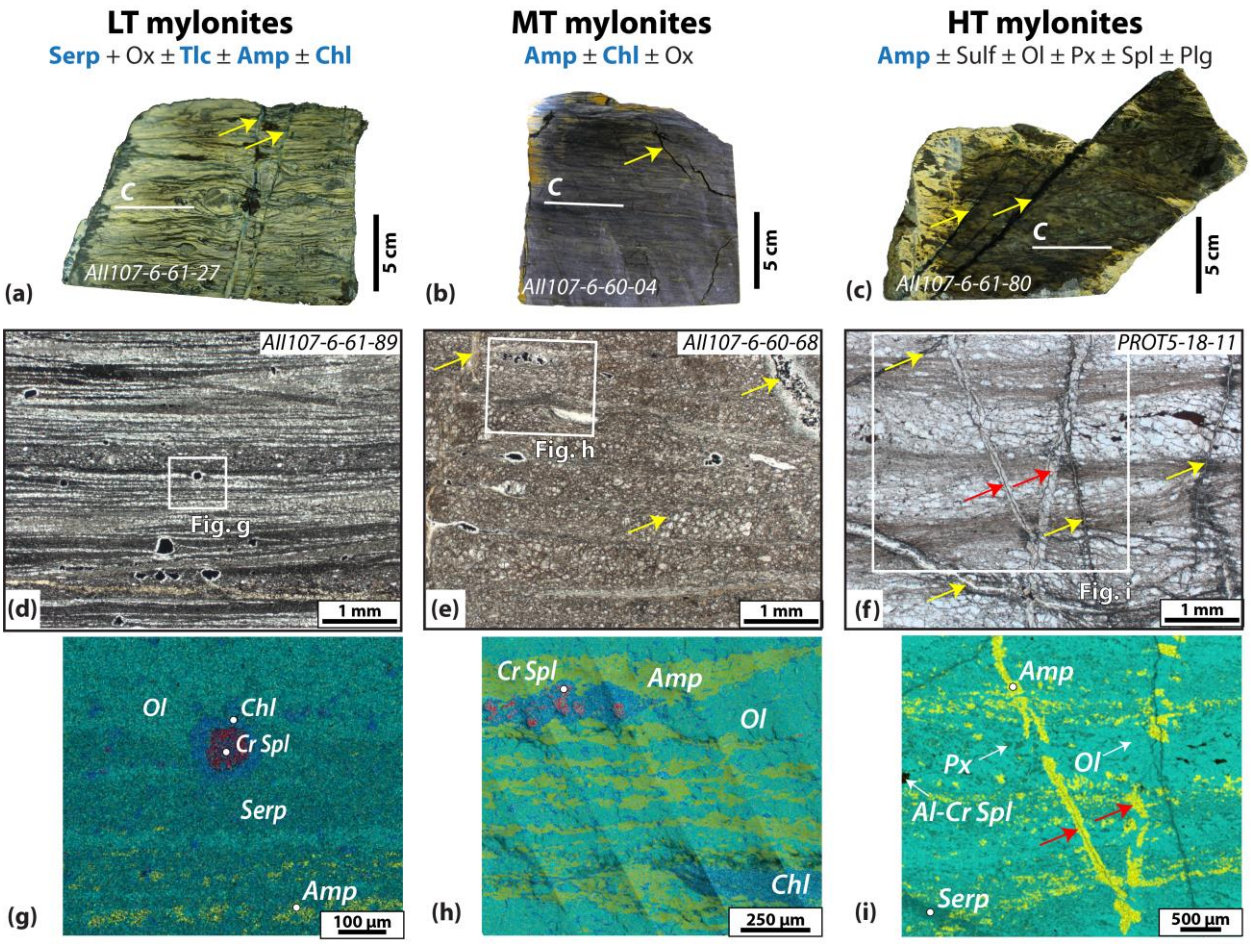

712

713 **Fig. 2.** Texture and mineralogy of low temperature (LT), medium-T (MT) and high-T (HT) mylonites.
714 Hand sample photographs are shown in a-c and optical photomicrograph in d-f. The white squares
715 show the location of EDS phase maps (g-i), which are colored to show the mineralogy. Samples have
716 been oriented with their shear planes (C, white line) horizontal. Fractures are indicated by yellow
717 arrows for LT fractures and red arrows for HT fractures. Amp: amphibole, Chl: chlorite, Ol: olivine,
718 Ox: oxide, Plg: plagioclase, Px: pyroxene, Serp: serpentine, Spl: spinel, Sulf: sulfide, Tlc: talc. Amp,
719 Chl, Serp, Tlc are hydrous phases.

720

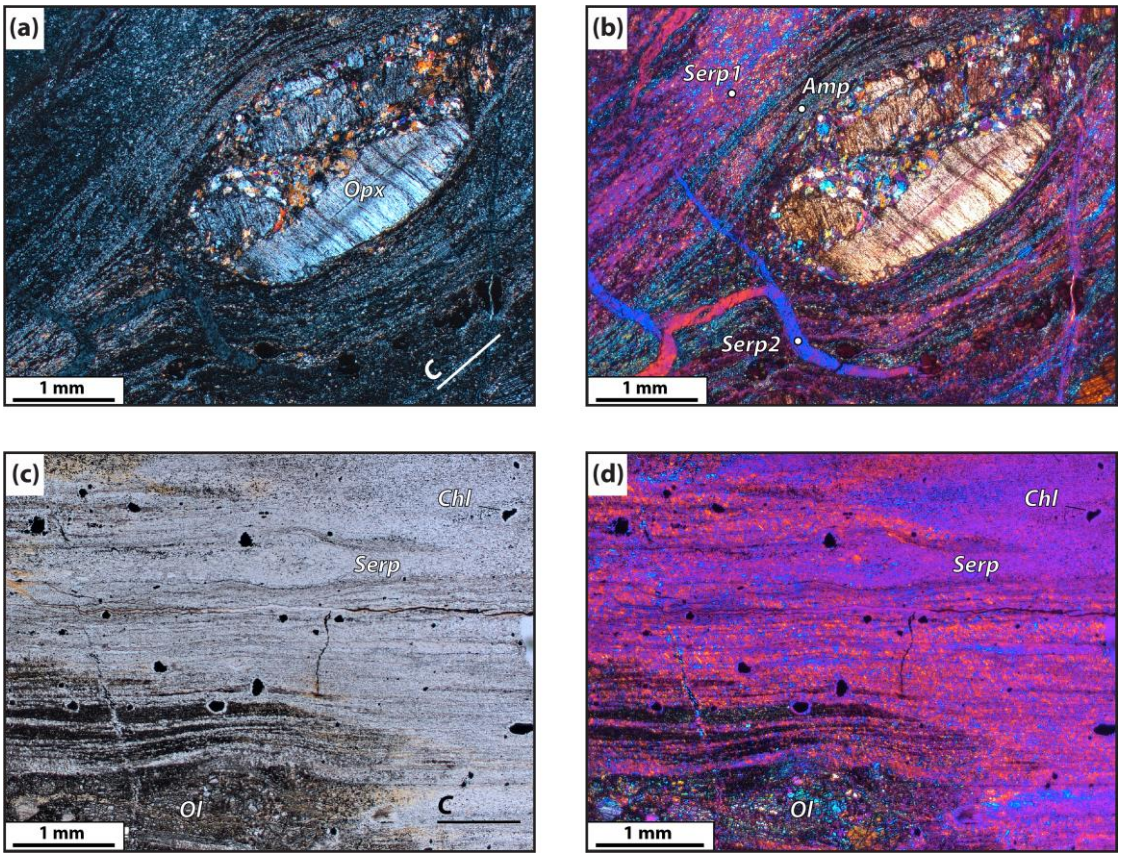

Fig.3. Textures in shear zones of LT mylonites. Optical photomicrographs in cross-polarized light (a) without and (b) with the addition of a wave plate for sample AII107-6-61-27. The wave plate is used to reveal the alternating serpentine (serp1)-rich (bright colors) and amphibole-rich (blues and grays) bands that are wrapped around an orthopyroxene porphyroclast. The mylonite matrix in this sample is composed entirely of serpentine and amphibole, which are interlayered, with neither phase replacing the other, suggesting textural equilibrium between these two phases. A later generation of serpentine (Serp2) crystallized in cross-cutting fractures. Optical photomicrograph in (c) plane-polarized light and (d) cross-polarized with the addition of a wave plate of LT mylonite sample AII107-6-61-89. Chlorite coronas are present around altered spinel in entirely serpentinized zones, indicating that both chlorite and serpentine can be co-stable in LT mylonites. In contrast, olivine (dark layers) is being replaced by serpentine, indicating dis-equilibrium between these phases.

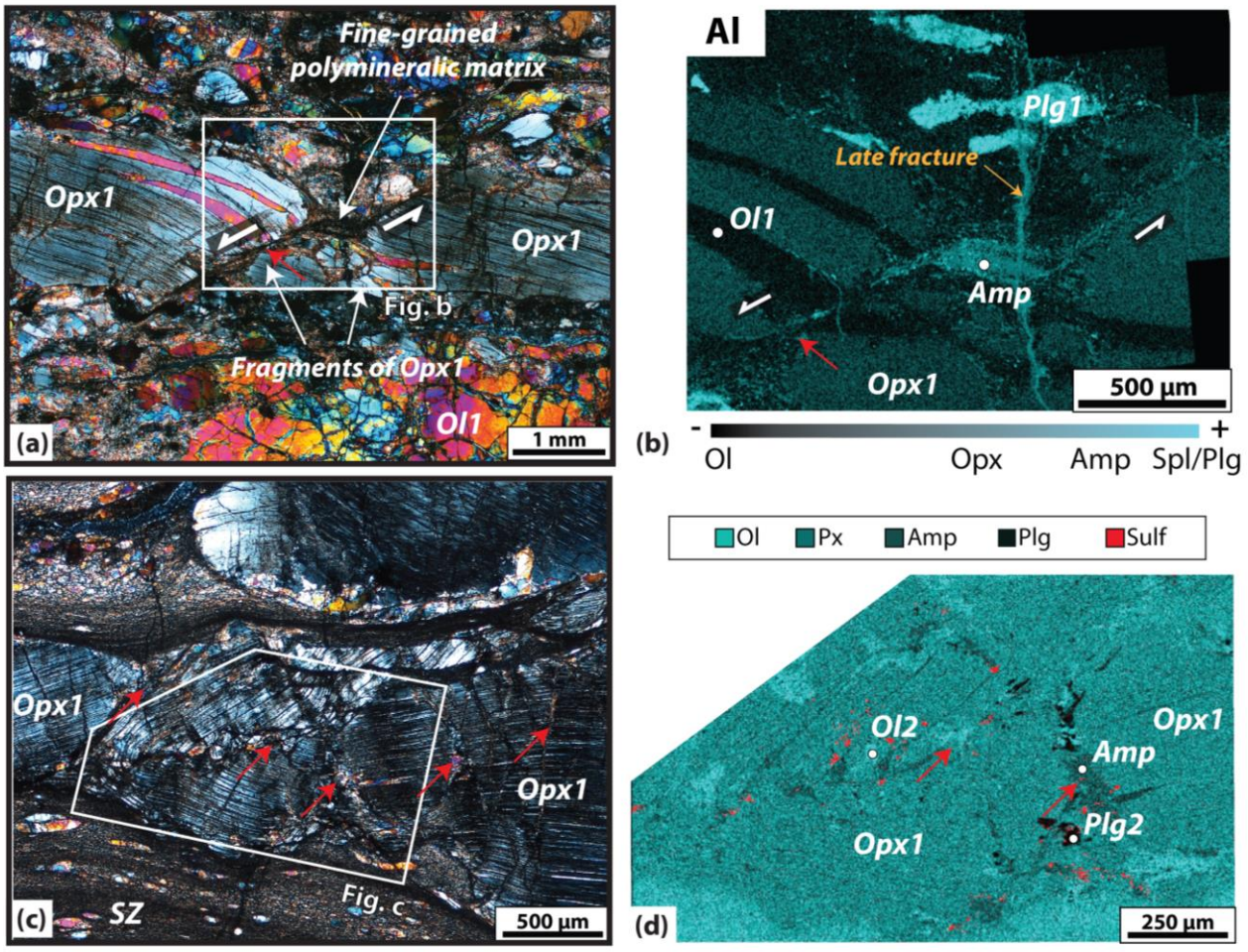

Fig. 4. Evidence for HT fracturing of porphyroclasts in (a-b) protomylonite PROT5-19-08 and (c-d) ultramylonite AII107-6-61-80. The white boxes on the polarized optical photomicrographs (a and c) indicate the location of the EDS maps (b and d). Red arrows point to fractures. The phases sealing the fractures are shown in (b) by the Al compositional map and in (d) by a phase map. Amp: amphibole, Ol: olivine, Opx: orthopyroxene, Plg: plagioclase, Px: pyroxene, Spl: spinel, Sulf: sulfide. Porphyroclasts and minerals in HT shear bands and fractures of the same phase are identified by 1 and 2, respectively.

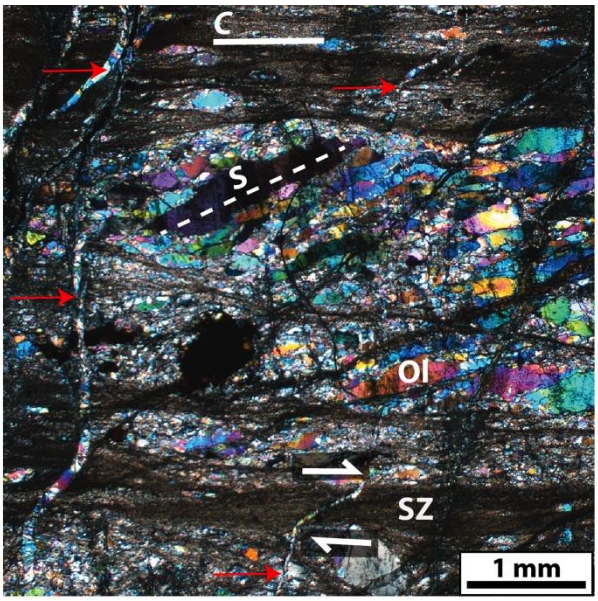

Fig. 5. Polarized optical photomicrograph showing transgranular fractures in a HT mylonite (PROT5-18-11). High temperature amphibole-bearing fractures are indicated by red arrows. These fractures subsequently underwent dextral shear offset, as shown by the white arrows for one of the fractures. The relationship between the shear plane (C, solid line) and the olivine (Ol) foliation (S, dashed line) also indicates a dextral sense of shear. Dextral senses of shear are relative to the thin-section structural reference frame.

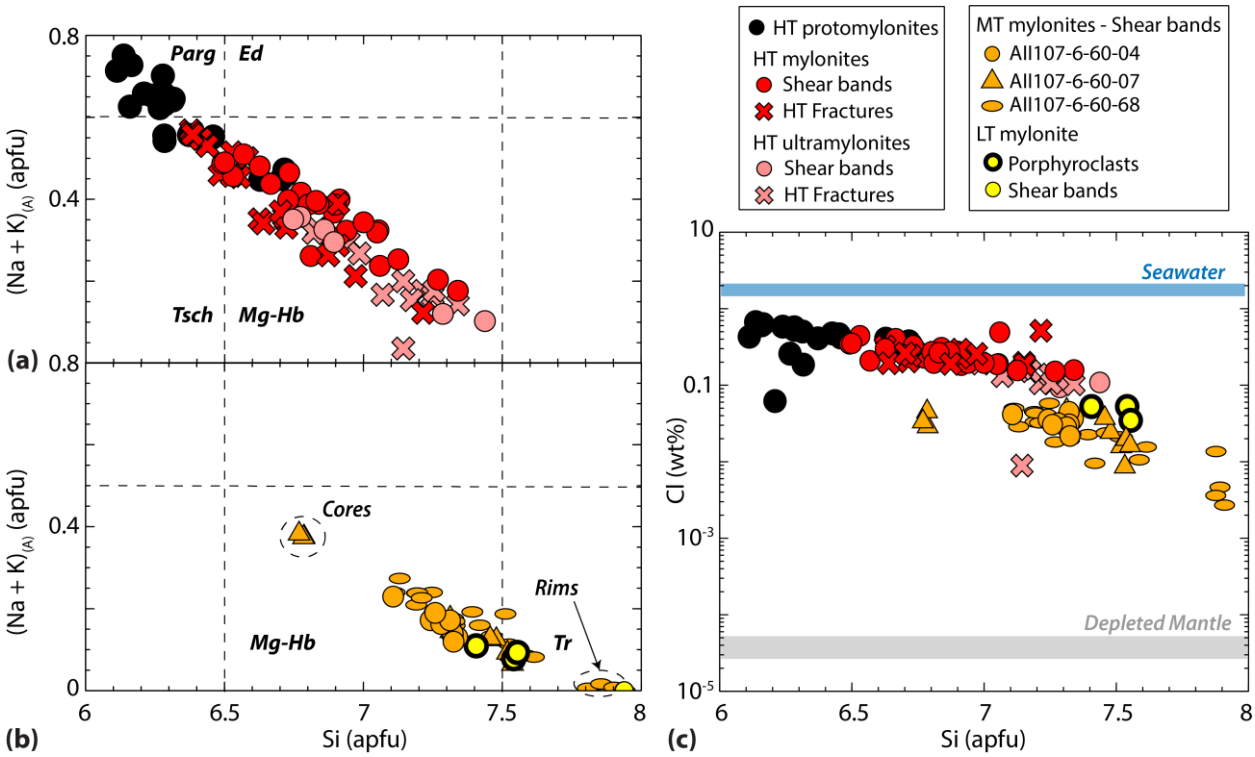

749

750 **Fig. 6.** Composition of amphibole in LT, MT and HT shear bands (circles) and fractures (crosses).

751 Alkali versus Si composition of amphibole in atom per formula unit (apfu) for (a) HT mylonites and

752 (b) MT and LT mylonites. The amphibole nomenclature is from Leake et al. (1997): edenite (Ed),

753 pargasite (Parg), magnesio-hornblende (Mg-Hb), tremolite (Tr), and tschermakite (Tsch). (c)

754 Amphibole Cl in wt% versus Si in apfu. The Cl concentration of the Depleted Mantle is from Urann et

755 al. (2017).

756

757

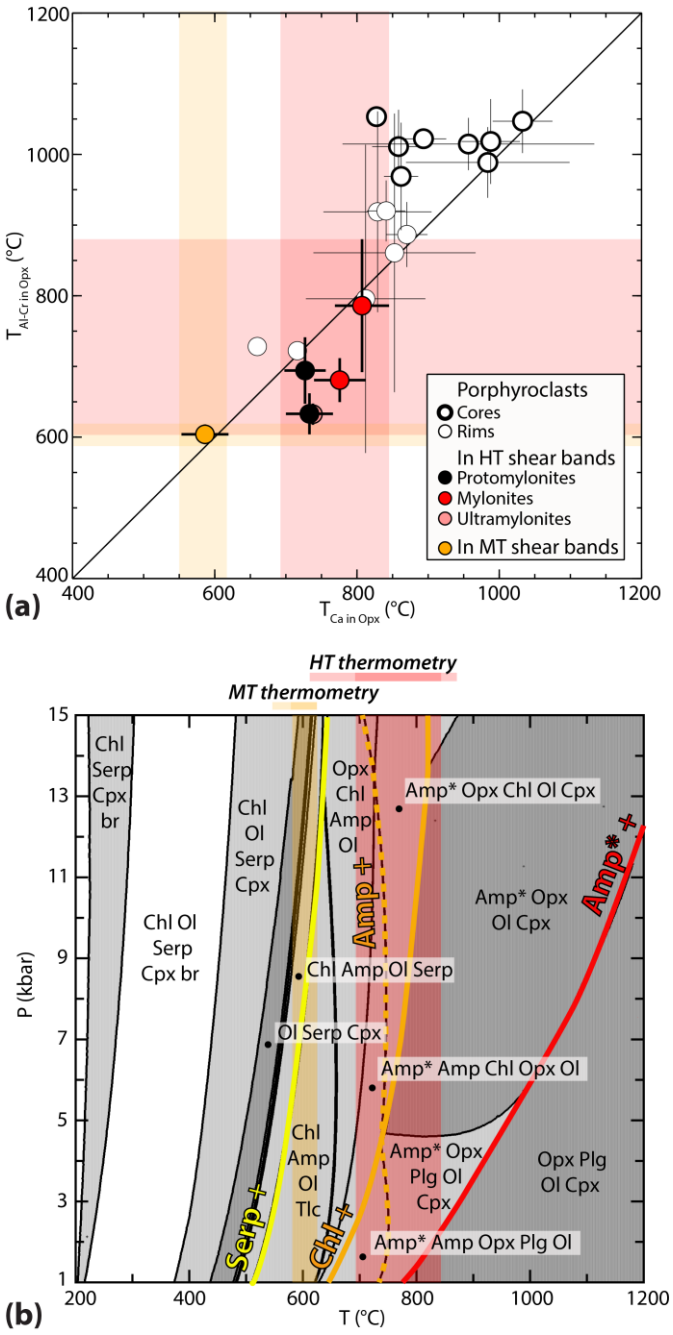

Fig. 7. Thermobarometry of HT, MT and LT mylonites. (a) Temperatures of porphyroclasts and grains in shear bands, based on orthopyroxene thermometry using $T_{Al\text{-}Cr\ in\ Opx}$ of Witt-Eickschen and Seck (1991) and $T_{Ca\ in\ Opx}$ of Brey and Köhler (1990). (b) Pseudosection constructed under water-saturated conditions using the composition of sample PROT5-19-08. The colored curves mark the upper stability limit of Pargasite to Mg-hornblende amphibole (red), chlorite (orange), tremolitic amphibole (dashed orange) and serpentine (yellow). Stability fields of hydrous phases in the OTF mylonites are mainly dependent on temperature. Amp: amphibole (tremolite), Amp*: amphibole (pargasite to Mg-

hornblende), Br: brucite, Chl: chlorite, Cpx: clinopyroxene, Ol: olivine, Opx: orthopyroxene, Plg: plagioclase, Px: pyroxene, Serp: serpentine, Spl: spinel, Tlc: talc.

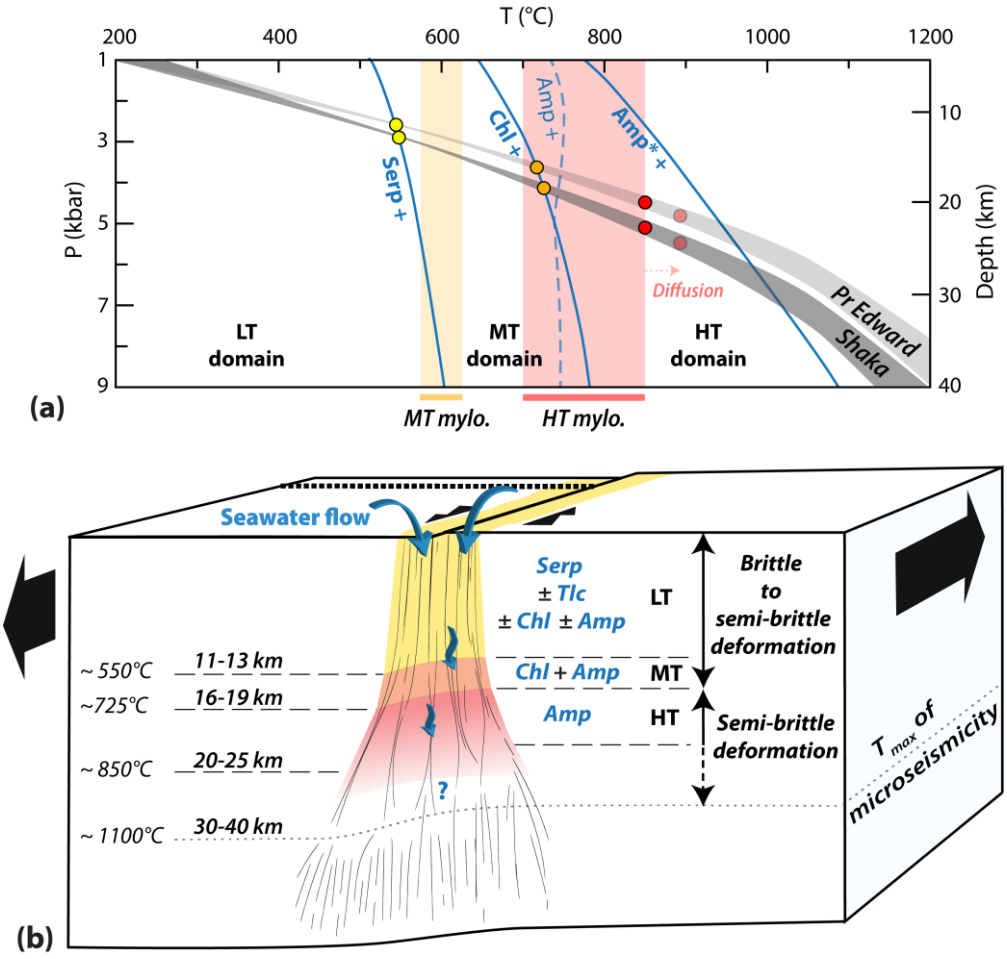

Fig. 8. Hydrothermal fluid percolation, fluid-rock interaction and mylonite formation on OTFs. a) Pressure-temperature domains of LT, MT and HT deformation (adapted from Fig. 6). The geotherm for the Shaka OTF (dark grey) is from a 3D viscoplastic thermomechanical model (see text), while the geotherm for the Pr Edward OTF (light grey) is calculated from earthquake scaling relations (eq. 7 of Wolfson-Schwehr et al. (2017)). b) Sketch summarizing our observations of deformation and fluid-mantle interaction on Shaka and Pr. Edward OTFs. The maximum temperature of microseismicity recorded on an OTF is from Roland et al. (2012).

Table 1. Location of dredges, rock type and deformation features of selected samples.

OTF	Cruise	Dredge #	sample #[1]	Rock Type	Deformation[2] HT (Amp)	MT (Chl + Amp)	LT (Serp)
Shaka	AII107-6	60	4	MT mylonite		B/D	B
			5	MT mylonite		B/D	B
			7	MT mylonite	B/D	B/D	B
			68	MT mylonite		B/D	B
		61	80	HT ultramylonite	B/D		B
			83	HT ultramylonite	B/D		B
			89	LT (ultra)mylonite		B/D	B/D
Pr Edward	PROT5	18	10	HT mylonite	B/D		B
			11	HT mylonite	B/D	B	B
		19	1	HT protomylonite	B/D	B	B
			8	HT protomylonite	B/D		B

1: Some samples were previously studied: AII107-6-61-83, PROT5-18-10 and PROT5-18-11 by Jaroslow et al. (1996), AII107-6-61-83 by Warren and Hirth (2006), and AII107-6-60-4, AII107-6-60-5, AII107-6-60-7 and AII107-6-61-83 by Kohli and Warren (subm).
2: Low temperature (LT) deformation domain is characterized by the presence of serpentine (Serp). Medium-T (MT) domain is marked by crystallization of chlorite (Chl) and tremolitic to Mg-hornblende amphibole (Amp). The high temperature (HT) domain is defined by crystallization of Mg-hornblende to pargasitic amphibole. D, B/D and B if the sample deformed in the deformation domain by ductile, semi-brittle or brittle mechanisms, respectively. A blank means that the sample has not experienced or has not preserved evidence of deformation within the corresponding deformation domain.

Table 2. Temperature estimates based on orthopyroxene (Opx) composition ($T_{Ca\ in\ Opx}$ of Brey and Köhler (1990) and $T_{Al\text{-}Cr\ in\ Opx}$ of Witt-Eickschen and Seck (1991)). The average temperatures are written in °C and the number of averaged grains is in parentheses.

Sample		Opx porphyroclasts core $T_{Ca\ in\ Opx}$	core $T_{Al\text{-}Cr\ in\ Opx}$		rim $T_{Ca\ in\ Opx}$	rim $T_{Al\text{-}Cr\ in\ Opx}$		Opx in shear zones $T_{Ca\ in\ Opx}$	Opx in shear zones $T_{Al\text{-}Cr\ in\ Opx}$	
HT protomylonites	PROT5-19-01	1033 ± 42	1047 ± 45	*(4)*	829 ± 76	919 ± 142	*(5)*	727 ± 29	694 ± 47	*(11)*
	PROT5-19-08	988 ± 41	1018 ± 60	*(4)*	853 ± 114	861 ± 197	*(7)*	733 ± 33	633 ± 29	*(12)*
HT mylonites	PROT5-18-10	862 ± 24	969 ± 76	*(5)*	841 ± 26	920 ± 43	*(4)*	807 ± 38	786 ± 94	*(15,*
	PROT5-18-11	893 ± 32	1022 ± 13	*(5)*	870 ± 29	887 ± 46	*(5)*	776 ± 35	681 ± 31	*(15)*
HT ultramylonite	AII107-6-61-80	984 ± 115	989 ± 50	*(3)*	812 ± 84	796 ± 218	*(3)*	738 ± 5	632 ± 15	*(4)*
MT mylonites	AII107-6-60-04	957 ± 178	1015 ± 37	*(3)*	660	728	*(1)*	586 ± 33	604 ± 14	*(7)*
	AII107-6-60-07	827	1053	*(1)*						
LT ultramylonite	AII107-6-61-27	858 ± 37	1011 ± 52	*(2)*	716	722	*(1)*			